

Maximizing fluorescence collection efficiency in multiphoton microscopy

Joseph P. Zinter¹ and Michael J. Levene^{1,*}

¹Department of Biomedical Engineering, Yale University, New Haven, CT 06511, USA

*michael.levene@yale.edu

Abstract: Understanding fluorescence propagation through a multiphoton microscope is of critical importance in designing high performance systems capable of deep tissue imaging. Optical models of a scattering tissue sample and the Olympus 20X 0.95NA microscope objective were used to simulate fluorescence propagation as a function of imaging depth for physiologically relevant scattering parameters. The spatio-angular distribution of fluorescence at the objective back aperture derived from these simulations was used to design a simple, maximally efficient post-objective fluorescence collection system. Monte Carlo simulations corroborated by data from experimental tissue phantoms demonstrate collection efficiency improvements of 50% – 90% over conventional, non-optimized fluorescence collection geometries at large imaging depths. Imaging performance was verified by imaging layer V neurons in mouse cortex to a depth of 850 μm .

©2011 Optical Society of America

OCIS codes: (180.0180) Microscopy; (180.2520) Fluorescence microscopy; (180.4315) Nonlinear microscopy; (220.0220) Optical design and fabrication; (220.4830) Systems design.

References and links

1. W. Denk, J. H. Strickler, and W. W. Webb, "Two-photon laser scanning fluorescence microscopy," *Science* **248**(4951), 73–76 (1990).
2. W. R. Zipfel, R. M. Williams, and W. W. Webb, "Nonlinear magic: multiphoton microscopy in the biosciences," *Nat. Biotechnol.* **21**(11), 1369–1377 (2003).
3. C. Xu and W. W. Webb, "Measurement of two-photon excitation cross sections of molecular fluorophores with data from 690 to 1050 nm," *J. Opt. Soc. Am. B* **13**(3), 481–491 (1996).
4. E. Beaurepaire, M. Oheim, and J. Mertz, "Ultra-deep two-photon fluorescence excitation in turbid media," *Opt. Commun.* **188**(1–4), 25–29 (2001).
5. P. Theer, M. T. Hasan, and W. Denk, "Two-photon imaging to a depth of 1000 microm in living brains by use of a Ti:Al₂O₃ regenerative amplifier," *Opt. Lett.* **28**(12), 1022–1024 (2003).
6. A. Leray, C. Odin, E. Huguet, F. Amblard, and Y. Le Grand, "Spatially distributed two-photon excitation fluorescence in scattering media: Experiments and time-resolved Monte Carlo simulations," *Opt. Commun.* **272**(1), 269–278 (2007).
7. A. Leray, C. Odin, and Y. Le Grand, "Out-of-focus fluorescence collection in two-photon microscopy of scattering media," *Opt. Commun.* **281**(24), 6139–6144 (2008).
8. P. Theer and W. Denk, "On the fundamental imaging-depth limit in two-photon microscopy," *J. Opt. Soc. Am. A* **23**(12), 3139–3149 (2006).
9. D. Kobat, M. E. Durst, N. Nishimura, A. W. Wong, C. B. Schaffer, and C. Xu, "Deep tissue multiphoton microscopy using longer wavelength excitation," *Opt. Express* **17**(16), 13354–13364 (2009).
10. S. G. Parra, T. H. Chia, J. P. Zinter, and M. J. Levene, "Multiphoton microscopy of cleared mouse organs," *J. Biomed. Opt.* **15**(3), 036017 (2010).
11. M. Oheim, E. Beaurepaire, E. Chaigneau, J. Mertz, and S. Charpak, "Two-photon microscopy in brain tissue: parameters influencing the imaging depth," *J. Neurosci. Methods* **111**(1), 29–37 (2001).
12. V. Tuchin, *Tissue Optics*, 2.ed., (SPIE, Bellingham, Washington, 2000).
13. E. Beaurepaire and J. Mertz, "Epifluorescence collection in two-photon microscopy," *Appl. Opt.* **41**(25), 5376–5382 (2002).
14. Y. Le Grand, A. Leray, T. Guilbert, and C. Odin, "Non-descanned versus descanned epifluorescence collection in two-photon microscopy: Experiments and Monte Carlo simulations," *Opt. Commun.* **281**(21), 5480–5486 (2008).

1. Introduction

Over the past 20 years, multiphoton microscopy (MPM) has established itself as the premier modality for high resolution, deep tissue, *in vivo* fluorescence imaging [1,2]. The dramatic improvements in imaging performance, when compared to confocal microscopy, result from the use of longer wavelength excitation light, and from the spatially and temporally localized generation of fluorescence. Since scattering length increases with wavelength, excitation in the near infrared allows a larger fraction of ballistic photons to reach the focus, thereby enabling excitation at greater depths than visible light. In addition, the nonlinear nature of multiphoton excitation makes the technique inherently optically sectioning, and eliminates the need for a confocal pinhole. This allows scattered fluorescence, normally rejected by a confocal pinhole, to be collected with the use of large area detectors, thereby increasing the total fraction of collected fluorescence, and consequently, the maximum imaging depth. As the technique continues to increase in popularity and utility, significant efforts are being made to push MPM to its limits in terms of maximum imaging depth. These approaches can be categorized into those aimed at increasing fluorescence excitation and those attempting to maximize fluorescence collection.

1.1 Maximizing fluorescence excitation

For an average excitation power, $\langle P \rangle$, the number of fluorescent photons generated per fluorophore per unit time, F_{gen} , can be expressed as [1,3]:

$$F_{gen} = \eta \frac{\sigma}{\tau f^2} \left(\frac{\pi (NA)^2}{hc\lambda} \right)^2 \langle P \rangle^2 e^{-2z/l_s^{exc}} \quad (1)$$

where η , σ , τ , and f , are the fluorophore quantum efficiency, two photon absorption cross-section, laser pulse duration and pulse repetition rate, respectively, NA is the objective numerical aperture, h is Planck's constant, and l_s^{exc} is the tissue scattering length at the excitation wavelength, λ . From Eq. (1), the relevant parameters for fluorescence generation can be compartmentalized into those pertaining to the laser (P , f , τ), laser focusing (NA), the sample (l_s^{exc} , z), and the fluorophore (η , σ , λ). From a laser perspective, Eq. (1) predicts large gains in F_{gen} by increasing $\langle P \rangle$, or smaller gains by decreasing the laser duty cycle, τf , both of which can be accomplished through regenerative amplification [4,5]. These approaches, however, are ultimately limited by the growth of fluorescence background arising from sources close to the tissue surface or by concerns of photo-damage to tissue [4,6–8]. In addition, they add significantly to system cost and complexity. Increasing the quality of the laser focus can be achieved by using high NA objectives, as is now common practice, however the upper bound for objectives appropriate for deep multiphoton imaging is approximately $NA = 1$. This limit results from the fact that objectives with numerical apertures greater than 1 typically have small front apertures, which drastically limits fluorescence collection (discussed below). The use of longer wavelength excitation, which effectively increases l_s^{exc} , has also been demonstrated; unfortunately, fewer fluorophores are available for multiphoton excitation at wavelengths greater than 1000 nm, and biological toxicity is more significant with these longer wavelength dyes [9]. A more direct approach to increase l_s^{exc} has recently been achieved through optical clearing of the tissue sample, and these methods have demonstrated multiphoton imaging to a depth of several millimeters, but they can only be employed *ex vivo* [10]. The final area for improving fluorescence generation is by way of optimizing fluorophore efficiency (η , σ), and is an area of active research.

1.2 Maximizing fluorescence collection

A second approach to increase imaging depth is to maximize the collected fraction of generated fluorescence. The total collected fluorescence, F_{coll} , can be expressed as:

$$F_{coll} = \phi(z, l_s^{fluor}, g^{fluor}, \theta_{sys}) \cdot F_{gen}(z, l_s^{exc}, P, \tau, f, \dots) \quad (2)$$

where $\phi(z, l_s^{fluor}, g^{fluor}, \theta_{sys})$ is defined as the fluorescence collection efficiency, which depends on the imaging depth, z , the scattering length, l_s^{fluor} , and scattering anisotropy, g^{fluor} , of the emitted fluorescence, and the angular acceptance of the microscope objective and the post-objective collection optics, θ_{sys} . From Eq. (2) it is evident that both the excitation and collection efficiency are a function of z , and that both ϕ and F_{gen} should be optimized in order to maximize the depth of imaging for MPM.

Although derivation of the functional form for ϕ is not straightforward, some general conclusions can be drawn. First, it is clear that the collection efficiency of the microscope objective scales like NA^2 . Second, it is known that the spatio-angular distribution of fluorescent photons emerging from a sample surface increases due to scattering, and therefore fluorescence collection can be greatly enhanced by using microscope objectives with large front apertures. For these reasons, the use of high NA and low magnification microscope objectives, such as the Olympus 20X 0.95NA objective (XLUMPLFLN 20XW, Olympus America, USA) used here, have become widespread and have resulted in dramatic improvements in collection efficiency [11]. It is also known that the varied spatial and angular distribution of these scattered fluorescent photons entering the objective front aperture (OFA) results in an angular distribution of fluorescence emerging from the objective back aperture (OBA), which we define as θ_f (Fig. 1). Since high- NA low-magnification objectives terminate in large OBAs, collecting the resulting angular distribution of fluorescence onto a detector photocathode requires careful optical design of the post-objective fluorescence collection system.

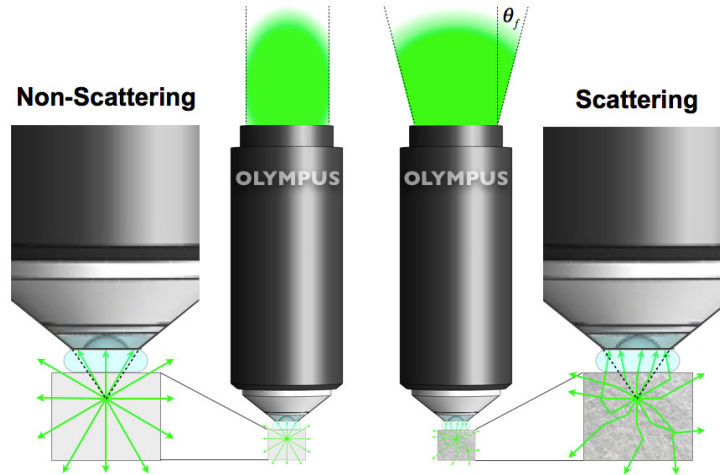


Fig. 1. Propagation of isotropically emitted fluorescent photons through a microscope objective for a non-scattering case (left) and scattering case (right). In the non-scattering case, photons that fall within the objective NA (illustrated as dashed lines) are collected, and emerge from the OBA in a collimated fashion. In the scattering case, photon trajectories are determined by the scattering properties of the sample. Scattering increases the total number of collected photons since photons that normally would not be collected can be scattered towards and enter the OFA. Scattered fluorescence entering the OFA results in a spatio-angular distribution of photons emerging from the OBA.

Unfortunately, an analytic expression for ϕ , and therefore θ_f , can only be achieved in the diffusive limit, that is, where the imaging depth, z , is much greater than the transport scattering length of the emitted fluorescence, l_t^{fluor} , defined as $l_t^{fluor} = l_s^{fluor} / (1 - g^{fluor})$. The transport scattering length is the photon path length at which a photon's trajectory becomes completely randomized. In brain tissue, l_s^{fluor} is on the order of 50 – 100 μm , with $g^{fluor} \approx 0.9$ for wavelengths near 500 nm [11,12]. This translates to transport scattering lengths of 500 – 1000 μm . Therefore, imposing the condition that $z \gg l_t^{fluor}$ presents an imaging scenario that cannot be achieved in practice, and thus, analytic expressions for ϕ are of little practical value.

To accurately determine the collection efficiency in the relevant (non-diffusive) regime, Monte Carlo simulations must be used. However, due to the complex trajectories of emitted fluorescent photons, Monte Carlo simulations can only be used effectively if the entire optical system, including the sample, microscope objective, and post-objective collection pathway are incorporated into the model. This poses a challenging problem since microscope objectives consist of a complex system of lenses whose configuration, geometry, and glass information are not readily available. Although previously published models have succeeded in accurately simulating photon propagation through scattering samples and the post-objective collection pathway, approximations have been used to model the microscope objective [7,11,13,14]. These approximations, in addition to the aforementioned assumptions placed on l_t^{fluor} , have caused previously published models to come to significantly different conclusions about the dependence of ϕ on z , with results ranging from a strong z^{-2} dependence, to a relatively weak exponential decay with increasing z [7,13,14].

To circumvent these issues, and to provide a more accurate model of fluorescence collection in MPM, we have simulated photon propagation through a scattering sample and a model of the Olympus 20X 0.95NA objective by way of Monte Carlo simulations. This information was used to generate the spatio-angular distribution of fluorescent photons emerging from the OBA, which allowed for an accurate determination of θ_f and provided the information necessary to optimize the design of the post-objective fluorescence collection optical path. Collection efficiency improvements were determined by comparing the resulting optimized design to conventional epi-collection geometries and common MPM photomultiplier tubes (PMTs), the H7422P-40mod GaAsP PMT (Hamamatsu, USA) and HC125-02 multi-alkali PMT (Hamamatsu, USA). Monte Carlo simulations corroborated by experimental data demonstrate collection efficiency improvements of 50% – 90% over typical, non-optimized optical configurations at imaging depths of 1000 μm . Furthermore, we conclude that the dependence of collection efficiency on image depth, z , is significantly affected by the post-objective collection optics and has a weak dependence on z in the case of an optimized design. Finally, we demonstrate *in vivo* imaging of layer V neurons expressing yellow fluorescent protein (YFP) in mouse cortex to a depth of 850 μm below the surface of the cortex.

2. Methods

2.1 Monte Carlo simulation methods

Embedded Monte Carlo routines in non-sequential Zemax optical design software (Zemax, USA) were used to model fluorescence propagation as a function of imaging depth in a scattering medium and to optimize collection geometries. The optical properties of the simulated scattering sample incorporated in the Monte Carlo model were chosen to match those which could be replicated in experimental tissue phantoms, and to span those typically found in *in vivo* multiphoton imaging of mammalian brain.

To model fluorescent photon propagation, a simulated source of constant power was embedded in a scattering volume over a depth range of 0 – 1200 μm in 25 μm increments. The rectangular volume source, 100 x 100 x 1 μm in dimension, was used to approximate an imaging field of view of 100 μm . Simulations used 5×10^5 rays emitted randomly and

isotropically from the source volume at a wavelength of 520 nm, corresponding to the peak emission wavelength of the fluorescent dye used experimentally. The Sobol sampling method was used in Zemax to define the random distribution. Three emission scattering lengths were chosen, 48.95, 73.43, 97.90 μm , with a corresponding emission anisotropy value of $g^{fluor} = 0.9254$ at a refractive index $n = 1.335$. These values span previously published values for mammalian brain at the specified emission wavelength [11,12]. The standard Henyey-Greenstein approximation was employed to define the angle of a scattered ray based on the prescribed value for g . Absorption was ignored since the experimental tissue phantoms used to verify the simulations had no absorptive power. Physiologically, this is also a reasonable assumption since the absorption coefficient in mammalian brain is over two orders of magnitude longer than typical scattering lengths, corresponding to an average photon path length of 2 mm before an absorption event [12]. The semi-infinite scattering volume, 10 x 10 x 10 mm, was bounded on its top surface by a 100 μm thick glass volume and then by a water volume to emulate the glass coverslip and immersion fluid used experimentally.

A critical step in fluorescence collection system design is to accurately determine flux and photon trajectory through the microscope objective. To do so, an optical model of the Olympus 20X 0.95NA objective was constructed using the data available in the U.S. Patent 6,501,603 B2 (Fig. 2). The spatial dimensions, curvature, and physical properties of all lenses and the objective front and rear apertures, including broadband anti-reflective magnesium fluoride (MgF_2) coatings, were modeled in Zemax to match the objective used experimentally.

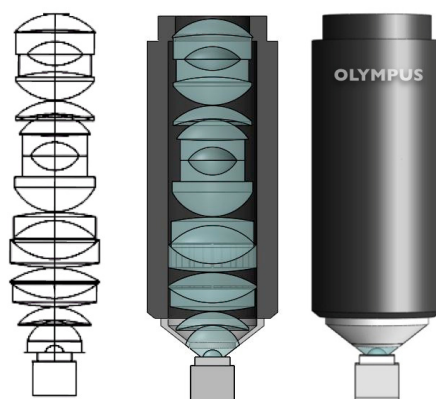


Fig. 2. Zemax schematic (left), and SolidWorks renderings (middle and right) of the Olympus 20X 0.95NA objective used for Monte Carlo simulations and opto-mechanical design.

Herein lies the major distinction between our work and prior art. Previous computational models of fluorescence collection by microscope objectives have used the criteria that a photon must strike the OFA and fall within the effective field of view in order to propagate through the optical system [7,11,13,14]. It is well known that the effective field of view of a microscope objective is much larger than the field of view specified by the objective manufacturer, and that this increase allows significantly more fluorescence to be collected [11]. The effective field of view can be measured experimentally by illuminating the back aperture of an objective with a collimated beam and measuring the transmittance as a function of angle of the input beam [11]. Due to the reciprocity of optics, this creates a scenario equivalent to photons emanating from an off axis point, as is the case for scattered fluorescent photons exiting the sample surface. This information can then be used to define a probability that photons from the off axis field point will propagate through the optical system. However, this experimental method inherently implies isotropic emission from every point on the sample surface, which, as discussed above, is only true in the diffusive limit, and is not an

accurate assumption for all images depths. Since we have modeled the complete microscope objective, the effective field of view is implicitly present in our model, and it is not necessary to impose any additional constraints. The combination of simulating a scattering sample and subsequent fluorescent photon propagation through a realistic model of a microscope objective allows for an accurate determination of photon trajectories at the OBA, which can then be used to design a maximally efficient post-objective fluorescence collection pathway.

2.2 *Opto-mechanical design*

Collecting the wide angular distribution of fluorescence emitted from the objective back aperture onto the photocathode of a PMT creates a challenging optical design scenario. This challenge is compounded further when one considers that PMTs with high quantum efficiencies also have small photocathodes, usually on the order of tens of square millimeters. The popular Hamamatsu H7422P-40mod GaAsP PMT, for example, has one of the highest quantum efficiencies in the visible range for a large-area photodetector, however, the relatively small (5 mm x 5 mm) and recessed nature of its photocathode results in a low angular acceptance of 22 degrees. Therefore, thoughtful design of the post-objective collection pathway is critical for efficient microscope design.

The physical constraints of our homebuilt multiphoton microscope, based on an Olympus BX51 corpus, and those of the aforementioned H7422P-40mod GaAsP PMT were loaded into the optical model. Zemax optimization routines were used to configure the post-objective fluorescence collection system within the physical constraints of our system. Virtual detectors were placed at various locations throughout the optical path to monitor photon throughput. Apertures, collection lenses, and the position of the H7422P-40mod GaAsP PMT were adjusted to maximize flux incident on the photocathode. We restricted the choice of collection lenses to those that were commercially available. Within this framework, we optically designed a two-channel fluorescence collection system that resides in the space immediately above the microscope objective, typically occupied by the fluorescence filter carousel. As expected, performance was greatly increased by maximizing the diameter of clear apertures, and correctly choosing and positioning collection lenses. A ray trace of the resulting optical system is presented in Fig. 3. The optically modeled system was then transferred to SolidWorks software (Dassault Systemes, USA) for mechanical design of the detector housing assembly, which is illustrated in Fig. 4.

The optimized fluorescence collection detector housing was designed and fabricated in-house using aluminum, brass, and off-the-shelf optical components and lenses. The assembly attaches to the microscope by way of the fluorescence filter carousel dovetail, providing easy installation and removal. The geometrical layout of the system, as depicted in Figs. 3 and 4 is as follows. A custom-made 40 mm x 57 mm 680 LP excitation/emission dichroic mirror (Chroma Technologies, VT) is situated at a 45 degree angle directly above the OBA yielding a center-to-center distance from the OBA of 58.45 mm. The plano surface of a large aperture, $d = 40$ mm, $f = 80$ mm, anti-reflective coated plano-convex lens (Lens 1) ($fb = 75.3$ mm) (O11-2570-A55, OptoSigma, USA) is positioned 21.51 mm from the dichroic mirror midpoint, for a total distance of 79.96 mm from the OBA. A standard size 25.4 mm x 36 mm, dichroic mirror placed after Lens 1 allows for simultaneous two-channel imaging. A second anti-reflective coated plano-convex lens, $d = 25.4$ mm, $f = 30$ mm, (Lens 2) ($fb = 24.2$ mm) (LA1805-A, ThorLabs, USA) is used on each leg of the two channel detection pathway to reduce the optical path length and focus fluorescence onto the photocathode of the Hamamatsu H7422P-40mod PMT. The distance between the convex surfaces of the two lenses is 88.19 mm, and the distance from the plano face of the second lens to the photocathode is 23.62 mm. Please refer to Fig. 3a for the orientation of Lens 1 and Lens 2. SM1 optical tubes (ThorLabs, USA) (not shown) are used to house band pass filters and Lens 2. For more information on the mechanical design, please contact the authors.

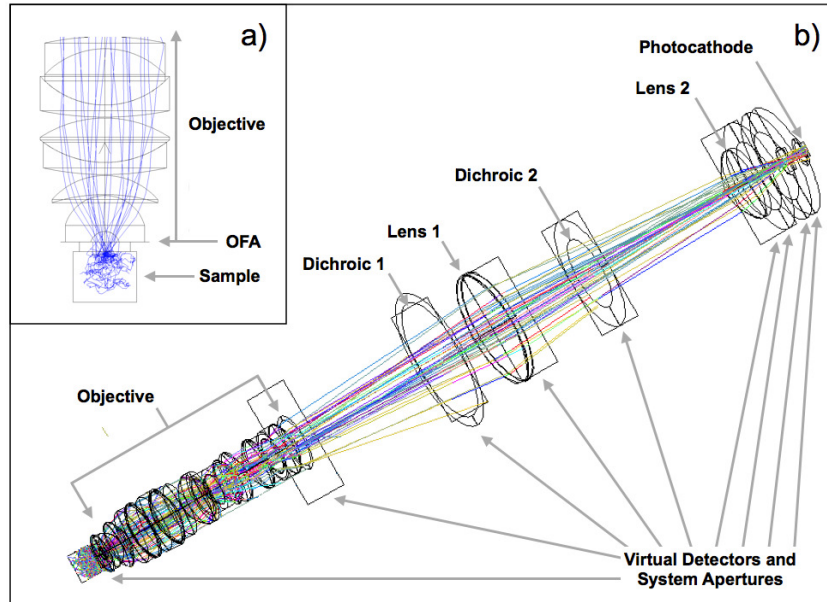


Fig. 3. Zemax Monte Carlo ray trace. a) Scattered photons (blue rays) propagating through a simulated scattering medium and entering the OFA of the Olympus 20X 0.95Na objective. b) Trimetric wireframe ray trace of the unfolded optimized post-objective fluorescence collection optical system. Rays exiting the scattering medium (left) travel through and emerge from the objective with an angular distribution. Collection lenses (Lens 1 and Lens 2) guide this fluorescence onto the PMT photocathode (right). Each ray segment is mapped to a different color. In both a) and b) rays exiting the optical system have been removed for clarity.

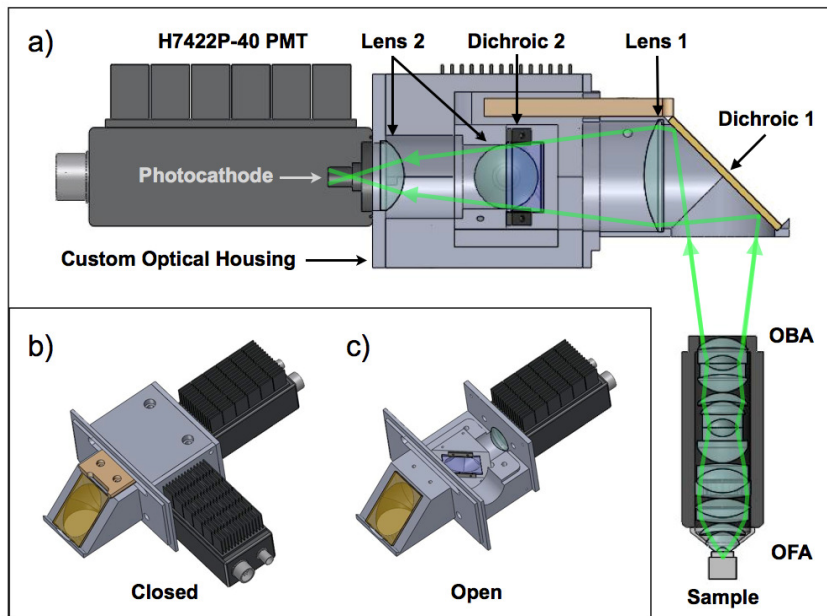


Fig. 4. Mechanical renderings of the optimized fluorescence collection system and detector housing assembly. a) Cutaway model of the microscope objective, detector housing, and H7422P-40mod GaAsP PMT. Green lines represent fluorescence propagation from the OBA to photocathode. Inset illustrations (b) and (c) show the closed detector housing assembly (b), and the same assembly with the top and one detector removed (c). SM1 optical tubes used to house the lenses and band pass filters have been removed to better illustrate function.

2.3 Tissue phantom experimental methods

Polystyrene microspheres were chosen as the scattering agent for our tissue phantoms due to their well-controlled particle size and refractive index. In addition, the uniformity and consistency of polystyrene microspheres allow scattering properties to be precisely calculated via Mie scattering theory. Although lipid based phantoms (milk, Intralipid, and Nutralipid) are often used to simulate the optical properties of tissue, we have found these systems to be unreliable for quantitative measurements owing to their varying distribution of particle sizes, particle aggregation, and irreproducibility of sample preparation.

Polystyrene microspheres (Polysciences Inc., USA) 0.974 μm in diameter were embedded in a 0.5% agarose gel matrix (Sigma-Aldrich Co., USA), and fluorescein dye (Sigma-Aldrich Co., USA) was added such that the final dye concentration was 10 μM . For an excitation wavelength of $\lambda = 800$ nm, the refractive index of polystyrene is $n = 1.5794$, and the refractive index of 0.5% agarose is $n = 1.3350$. These parameters, along with the particle diameter, allowed microsphere concentrations to be calculated via Mie theory to produce samples with excitation scattering lengths of 100, 150, and 200 μm at 800 nm, with a corresponding excitation anisotropy of $g^{\text{exc}} = 0.8991$. As stated earlier, scattering lengths were chosen to span those typically found in mammalian brain at the given excitation wavelength, and match the emission scattering properties of the Monte Carlo simulations [11,12]. The above concentrations yielded emission scattering lengths of 48.95, 73.43, and 97.9 μm , with an emission anisotropy of $g^{\text{fluor}} = 0.9254$ at 520 nm, corresponding to the fluorescence emission peak of fluorescein. Henceforth, for simplicity, these emission scattering lengths will be approximated as 50, 75, and 100 μm . Microsphere concentrations and subsequent scattering properties are summarized in Table 1.

Table 1. Tissue Phantom Scattering Properties.

Concentration (microspheres/mL)	l_s^{exc} (μm) $\lambda^{\text{exc}} = 800$ nm, $g^{\text{exc}} = 0.8991$	l_s^{fluor} (μm) $\lambda^{\text{fluor}} = 520$ nm, $g^{\text{fluor}} = 0.9254$
8.53×10^9	100	48.95 (~50)
5.69×10^9	150	73.43 (~75)
4.27×10^9	200	97.90 (~100)

To ensure a flat and optically transparent imaging surface, custom sample chambers were constructed. Holes were drilled through the bottom of a 24-well plastic plate, and #1 coverslips were glued to the top. Prior to polymerization, the well plate was inverted and loaded with the agarose mixture, and the bottom was sealed to prevent evaporation.

The tissue phantoms were imaged on a homebuilt multiphoton microscope, with 800 nm excitation provided by an 80 MHz pulsed Ti:sapphire laser (Mai Tai, Spectra Physics, USA). As stated earlier, the microscope system consisted of an Olympus 20X 0.95NA microscope objective coupled to two Hamamatsu H7422P-40mod PMTs via the custom housing. This housing incorporated a custom, large-aperture 680 DCXRU long pass dichroic mirror (Chroma, USA) to separate excitation and emission, and to divert fluorescent signal through an HQ 525/50 bandpass filter (Chroma, USA). Images we recorded from 0 – 1200 μm in 2 μm increments, with a field of view of 100 μm . The average pixel value after background subtraction of the 512 x 512 images was used as the measure of fluorescent signal. Background was taken to be the average pixel value at an imaging depth of 1.8 mm, where, due to the exponential falloff of ballistic photons with depth, zero fluorescence excitation is expected to occur. To ensure accurate determination of the sample surface, scans were initiated approximately 50 μm above the sample surface, and the image with the maximum average pixel value was defined as depth $z = 0$.

2.4 In vivo imaging methods

To verify imaging performance, the layer V neurons of a Thy1-YFP + P30 mouse were imaged *in vivo* with our optimized fluorescence collection system. The mouse was

anesthetized with an intraperitoneal injection of ketamine (100 mg/kg) and xylazine (10 mg/kg), and immobilized in a stereotactic mount. Body temperature was regulated using a 36°C water filled heating pad. Upon exposing the skull, a 4-mm craniotomy was performed over the cortex using a dental burr. To minimize the potential for bleeding, the dura was allowed to remain intact. The region was then soaked in phosphate buffered saline (PBS), which also acted as an immersion medium for imaging experiments. All images were acquired at an excitation wavelength of 886 nm, using a 550/88 band pass filter (Semrock, USA). The above procedure was approved by the Yale University Institutional Animal Care and Use Committee.

3. Results and discussion

3.1 Monte Carlo simulation results

Using the parameters described earlier, Monte Carlo simulations were performed for three scattering lengths at imaging depths ranging from 0 – 1200 μm . For a constant power fluorescent source at 520 nm, Fig. 5a depicts the total amount of fluorescence striking the modeled Olympus 20X 0.95NA OFA and emerging from the OBA for emission scattering lengths of 50, 75, and 100 μm , with imaging depth normalized to emission scattering length. For reference, the amount of fluorescence collected by an objective for a non-scattering sample would be $(1 - \cos\theta_{NA})/2$, which, for the objective modeled here, equates to 15% of the total fluorescence, independent of imaging depth. This value is illustrated as a black dashed horizontal line in Fig. 5a. There is a significant increase in photon flux across the OFA compared to the non-scattering case. Scattering enables photons that would otherwise not strike the OFA to be redirected towards the OFA, as illustrated in Fig. 1. Although this scattering enhancement has been identified by others, it is worth reiterating here since it contributes to one of the major advantages of MPM over confocal microscopy [13]. The absence of a confocal pinhole in MPM not only allows scattered photons to be collected as usable signal, but when the sample is sufficiently thick we also see nearly a two-fold increase in the amount of fluorescence entering the OFA over the non-scattering case. This result suggests that it is advantageous to image thicker, rather than thinner scattering samples [13]. In addition, we find that the number of photons striking the OFA increases with decreasing sample scattering length, and is a relatively constant function after an imaging depth of approximately 2 scattering lengths.

Since a microscope objective is only capable of transmitting photons that fall within a given spatio-angular acceptance, the fraction of total fluorescence which emerges from the OBA is significantly less than one, however, the transmitted intensities for the physiologically relevant scattering lengths evaluated here often meet or exceed those expected for the non-scattering case. It is often assumed that the ability to collect fluorescence drops precipitously with depth in scattering samples, here, we demonstrate that this is not the case.

To understand the spatial and angular dependence of intensity emerging from the OBA as a function of depth, we have evaluated the intensity at an aperture placed 58.45 mm from the OBA, for surface ($z = 0 \mu\text{m}$) and deep ($z = 1000 \mu\text{m}$) imaging. Since our optical model was designed in accordance with the spatial constraints of our MPM, this distance represents the minimum allowable distance between the midpoint of the excitation/emission dichroic mirror and the OBA when the size of the dichroic mirror was maximized. This position allowed for a dichroic mirror with a clear aperture of 38 mm. Figure 5b illustrates the collected fraction of fluorescence emerging from the OBA as a function of θ_f , as defined in Fig. 1. Vertical lines represent the collected intensity at this evaluation location for a clear aperture of 23 mm (typical for 1 in. optics) and the large 38 mm clear aperture used in our experimental system. For near-surface imaging there is a small increase in collected fluorescence of approximately 5% for the three scattering lengths, indicating the majority of the fluorescence emerging from the OBA does so in a roughly collimated fashion. However, for large imaging depths, there is an increase in the collected fraction of fluorescence ranging from 20% – 32%, depending on scattering length, for a 38 mm clear aperture over the standard 23 mm clear aperture. In

addition, there are only small gains in collected fluorescence beyond the 38 mm aperture, suggesting that a well-optimized post-objective fluorescence collection system should have a θ_f of ~ 10 degrees.

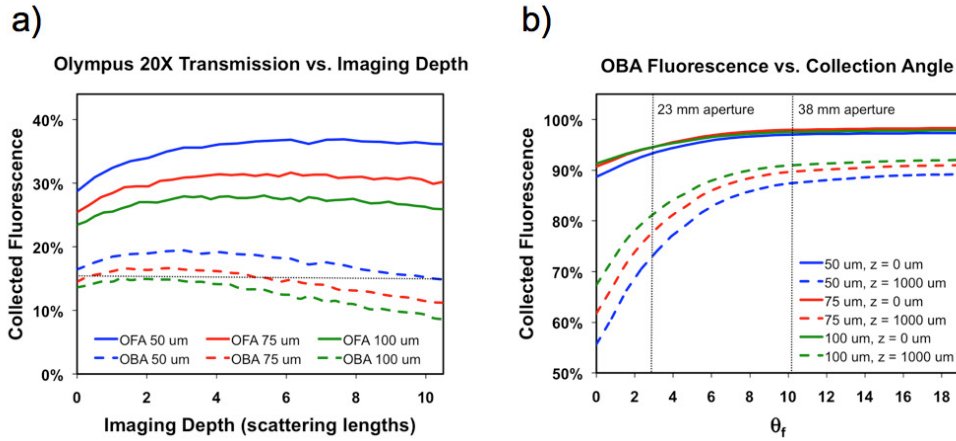


Fig. 5. Zemax Monte Carlo simulations for fluorescence propagation through the Olympus 20X 0.95NA microscope objective. a) Collected fraction of total fluorescence emitted from an isotropic source as a function of depth for emission scattering lengths of 50, 75, and 100 μm , normalized to emission scattering length. Solid color lines represent photon flux incident at the OFA. Dashed color lines represent the transmitted intensity measured at the OBA for the three scattering cases. The horizontal dashed line indicates the collected and transmitted fluorescence without scattering assuming an NA = 0.95. b) Collected fraction of fluorescence emerging from the OBA as a function of collection angle for emission scattering lengths of 50, 75, and 100 μm , for surface ($z = 0 \mu\text{m}$) and deep ($z = 1000 \mu\text{m}$) imaging. Vertical dashed lines correspond to a standard 23 mm and custom 38 mm clear aperture at the evaluation location described in the text.

Using the simulated intensity distributions at the OBA, optimization of the post-objective collection pathway was performed in Zemax. The constraints imposed on our design were to maximize the photon flux incident on the photocathode of the Hamamatsu H7422P-40mod PMT using off-the-shelf optical components. In addition, we required simultaneous two-channel imaging. Thus, spatial limitations were partially dictated by the proximity with which two PMTs could be placed at 90 degrees with respect to each other. The result was the post-objective fluorescence collection system illustrated in Fig. 3 and 4 consisting of two plano-convex lenses; a large 40 mm clear aperture lens (Lens 1) placed as close as possible to the excitation/emission dichroic mirror, and a second 25.4 mm lens (Lens 2) in close proximity to the PMT.

Figure 6b illustrates the results of a Zemax Monte Carlo simulation of fluorescence propagation through our optimized fluorescence collection system as a function of depth for a sample with an emission scattering length of 100 μm . Here, photon flux has been evaluated at each of the system apertures, which include the OFA, the OBA, the custom large aperture dichroic mirror (Dichroic), Lens 1, Lens 2, and the Hamamatsu H7422P-40mod photocathode (Detector), as illustrated in Fig. 6a. For the optimized collection geometry, the shape of the function for collected fluorescence follows that of the OBA with small losses at each system aperture, and larger losses at the detector due to the small and recessed photocathode.

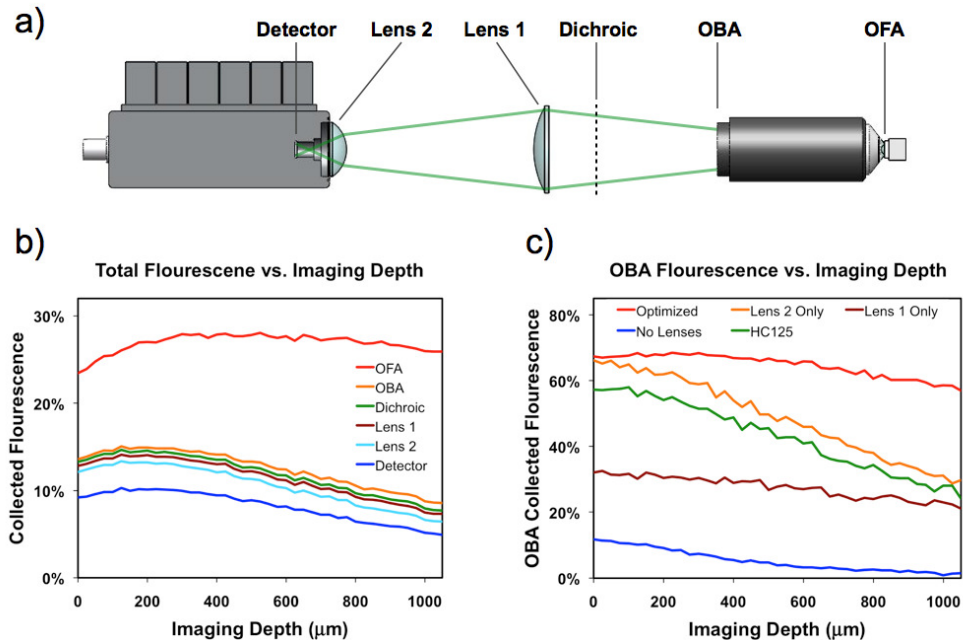


Fig. 6. Monte Carlo simulations of optimized and non-optimized fluorescence collection system performance. a) Unfolded optimized fluorescence collection system. b) Fraction of total fluorescence collected for the optimized housing design as a function of imaging depth evaluated at each system aperture. c) Comparison of fluorescence striking the PMT photocathodes for optimized and conventional geometries, normalized to the fluorescence emerging from the OBA. See text for description of geometrical configurations. Data in this figure pertains to a sample with an emission scattering length of $100 \mu\text{m}$ at 520 nm .

To determine the improvement in fluorescence collection of our optimized collection system over more conventional home-built collection systems, we evaluated 4 additional post-objective geometries. Two common configurations for fluorescence collection are as follows: 1) Hamamatsu HC125-02 PMTs placed as close as possible to the OBA using 23 mm clear apertures and no collection lenses (referred to in Fig. 6c as “HC125”), and 2) Hamamatsu H7422P-40mod PMTs placed as close as possible to OBA with a 25.4 mm lens placed f_1 away from the detector (referred to in Fig. 6c as “Lens 2 only”). For completeness, we have also evaluated collection geometries consisting of our large aperture lens with no additional lenses (“Lens 1 only”), and a scenario with no collection lenses (“No Lenses”), for the Hamamatsu H7422P-40mod PMT. Figure 6c illustrates the performance of the aforementioned geometries compared to our optimized post-objective collection system for a sample with an emission scattering length of $100 \mu\text{m}$, where the fluorescence for each configuration has been normalized to that emerging from the OBA. Although slight variations certainly exist between real world configurations and those modeled here, results are significant enough to conclude that optimized designs far exceed the performance of more conventional geometries.

For near surface imaging, collection of fluorescence emerging from the OBA onto the H7422P-40mod photocathode for the optimized geometry is $\sim 70\%$, and remarkably constant, falling by less than 10% over the entire imaging depth range of $0 - 1000 \mu\text{m}$. The “Lens 2 only” case demonstrates similar near-surface performance, which is expected since most of the fluorescence emerging from shallow imaging depths exits the OBA in a roughly collimated fashion as shown in Fig. 5b. However, as imaging depth increases, the angular distribution of fluorescence from the OBA increases, and subsequently we notice a significant linear decrease in collection efficiency for the “Lens 2 only” case.

The HC125 configuration, which uses no collection lenses, provides similar performance to the “Lens 2 only” case. Here, it is worth noting that the photocathode of the HC125 PMT is 21 mm in diameter, yielding an active area approximately 14 times larger than the photocathode of the H7422P-40mod PMT. However, the H7422P-40mod PMT has a quantum efficiency which is approximately 4 times higher than the HC125 PMT, so one would require 3.5 times more fluorescence to strike the photocathode of the HC125 PMT to provide similar performance to the H7422P-40mod PMT. Figure 6c only demonstrates the photon flux across the photocathode for the two PMTs, and does not take into account the difference in quantum efficiencies. Thus, not only do the optimized and “Lens 2 only” configurations place significantly more photons on the much smaller photocathode in an absolute sense, the H7422P-40mod PMTs also provide 4 times the efficiency in terms of photon conversion to usable signal. We stress this point here, since many home-built MPMs use HC125 PMTs (or similar), because it is sometimes assumed that the small and recessed nature of the H7422P-40mod photocathode will result in smaller signal even with the large quantum efficiency advantage. Here, we demonstrate that a simple plano-convex lens placed f1 in front of the detector will overcome this problem, and that further and significant gains in fluorescence collection efficiency can be achieved with an optimized, two-lens collection system.

Also illustrated in Fig. 6c is the photon flux incident on a H7422P-40mod photocathode with no collection lenses, and with one large aperture lens (Lens 1 only). As expected, the performance for the “No Lens” case is poor. Interestingly, the “Lens 1 only” case demonstrates a relatively constant collection efficiency with increasing imaging depth, similar to the optimized configuration, albeit at approximately half that of the optimized case. As demonstrated in Fig. 5b, a large aperture placed close to the OBA is required to efficiently collect the wide angular distribution of emergent fluorescence. Simply stated, the large aperture lens is responsible for collecting and concentrating the wide angular distribution of fluorescence emerging from the OBA onto Lens 2, which focuses this fluorescence onto the photocathode, resulting in highly efficient fluorescence collection at the photocathode that is relatively constant with increasing imaging depth. In all of the above configurations, the distance between the photocathodes and OBA was equal.

3.2 Tissue phantom experimental results

The optimized optical design of the post-objective collection pathway was transferred to SolidWorks mechanical design software and mechanical designs were created to physically house the optical elements prescribed by the optical models. The optimized housing was manufactured in house, and its performance was experimentally verified using fluorescent tissue phantoms consisting of fluorescein dye and 0.5% agarose gel embedded with polystyrene microspheres. As described above, tissue phantoms were developed to match the wavelength and scattering properties of the Monte Carlo simulations. To experimentally verify scattering properties, phantoms with emission scattering lengths of 50, 75, and 100 μm at 520 nm (corresponding to excitation scattering lengths of 100, 150, and 200 μm , respectively, at 800 nm) were imaged using a constant power of 25 mW at 800 nm and fixed detector gain. Figure 7a shows a logarithmic plot of the average pixel intensity after normalization and background subtraction for the three scattering phantoms as a function of imaging depth. Since only ballistic photons contribute to fluorescence generation, one can calculate the scattering length of the sample using:

$$P = P_0 e^{-z/l_s^{exc}} \quad (3)$$

Exponential fits reveal excitation scattering lengths of 112, 156, and 208 μm with R^2 values of 0.998, 0.997, and 0.999, respectively, matching expected Mie theory values (and Monte Carlo simulations) of 100, 150, and 200 μm to within 12.0, 4.0, and 4.0%, respectively. Having effectively established tissue phantoms with the desired scattering properties, we characterized the increase in imaging performance of an optimized vs. non-optimized collection geometry for a scattering phantom with an emission scattering length of 100 μm . For the non-optimized case, we evaluated the “Lens 2 only” configuration versus the

two-lens optimized design. Using the methods described above, images were acquired at 2 μm intervals over a range of 0 – 1200 μm with a fixed detector gain at an excitation wavelength of 800 nm. In order to maintain an adequate level of detectable fluorescence signal, the excitation power at the sample was doubled every 200 μm in the following manner: 25, 50, 100, 200, 400, and 480 mW, where 480 mW represents the maximum power at the sample our system could provide.

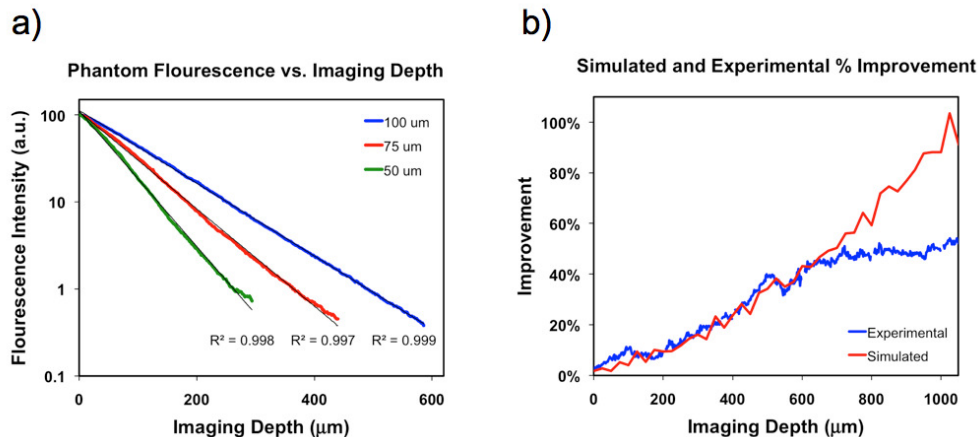


Fig. 7. Experimental tissue phantom performance. a) Fluorescence signal as a function of depth for tissue phantoms with emission scattering lengths of 50, 75, and 100 μm at 520 nm (corresponding to excitation scattering lengths of 100, 150, and 200 μm , respectively, at an excitation of 800 nm). Exponential fits are used to determine actual scattering properties (see text). b) Percent improvement in fluorescence collection as a function of depth for the optimized vs. “Lens 2 only” configuration.

Figure 7b demonstrates the percent improvement in collected fluorescence signal as a function of depth for the optimized vs. non-optimized design after background subtraction. There is remarkable conformance between the simulated and experimental data up to ~600 μm in imaging depth (6 emission scattering lengths), at which point improvement in the experimental case begins to grow more slowly, reaching a maximum of approximately 50% at an imaging depth of 1000 μm (10 emission scattering lengths). Growth in fluorescence background from the phantom surface due to large excitation intensities is responsible for the deviation from simulated gains. Simulations predict nearly a 100% improvement in fluorescent signal at a depth of 1000 μm . Since $F \propto P^2$, this gain is equivalent to increasing the excitation power at the sample surface by ~41%. Similarly the experimental gain in signal of approximately 50% equates to an increase in excitation power of ~22%. It is clear that optimized fluorescence collection systems allow for a substantial reduction in required excitation power. This decrease in power results in less fluorescence background from superficial depths and decreased photodamage when using large excitation intensities, as is typical for deep tissue imaging.

3.3 *In vivo* imaging results

To demonstrate how the fluorescence collection gains translate into an increase in imaging performance and depth, a Thy1-YFP + P30 mouse was imaged using the protocol described above. Using an excitation wavelength of 886 nm, 500 images were recorded at 2 μm intervals. The excitation intensity was adjusted manually such that the visualized fluorescent signal was approximately constant throughout the imaging depth. A maximum intensity cross-sectional (*y-z*) projection of a 1000 μm image stack is presented in Fig. 8a. The surface was defined as the point at which the dendritic arbor first became visible. Layer V cell bodies were visible to a depth of 850 μm . Figure 8b and 8c demonstrates a comparison of the optimized

fluorescence collection system using the Hamamatsu H7422P-40mod PMT and a non-optimized system consisting of no lenses and using the Hamamatsu HC125-02 PMT. These images represent a maximum intensity z-projection of 50 images over a depth range of 750 to 850 μm , with a field of view of 175 μm . Both imaged stacks were recorded using fixed detector gains and at the same excitation power. In an effort to provide a reasonable and fair comparison, the background of the images was equalized using the average pixel value over a region containing no cell bodies. White levels were then adjusted such that each image contains the same upper and lower threshold. Figure 8d and 8e represent a 3.5X zoom of a cell body from Figs. 8b and 8c, with a corresponding field of view of 50 μm . Significant gains in image contrast and resolution are clearly visible in the optimized fluorescence collection system.

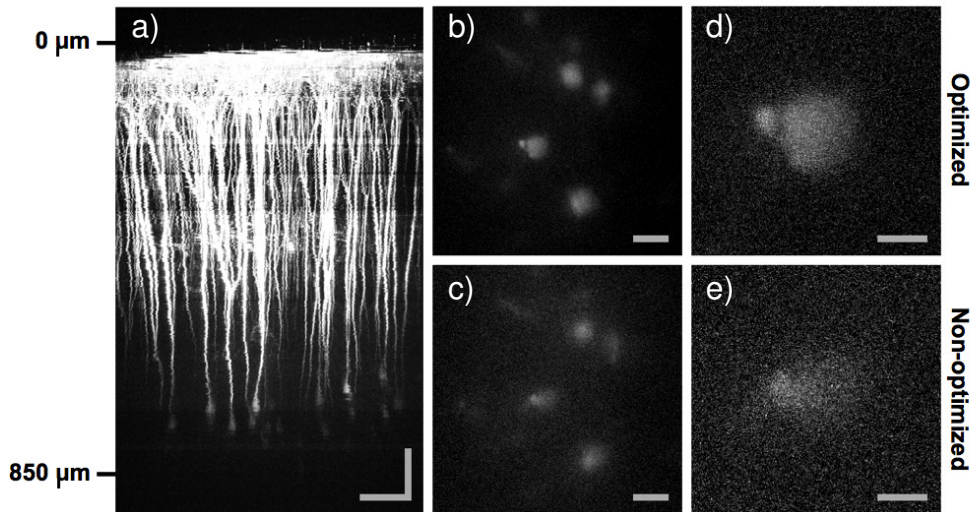


Fig. 8. *In vivo* imaging of Thy1-YFP + P30 mouse cortex. a) Cross-sectional maximum intensity (y-z) projection of a 1000 μm stack containing 500 1024 x 1024 images collected at 2 μm intervals. Scale bar = 100 μm . b) and c) Layer V cell bodies illustrated by way of a maximum intensity z-projection of 50 images from a depth of 750 – 850 μm for an optimized (b) and non-optimized (c) fluorescence collection system. Scale bar = 25 μm . c) and d) 3.5X zoom of a layer V cell body from images (b) and (c), respectively. Scale bar = 10 μm .

4. Conclusions

Optimization of the fluorescence collection pathway is a critical, yet often overlooked aspect of multiphoton microscope design. Here, we have optically modeled fluorescence propagation through a scattering sample with relevant physiologic and multiphoton imaging parameters. Photons exiting this scattering model and propagating through a model of the Olympus 20X 0.95NA objective were used to determine the spatio-angular distribution of light emerging from the OBA as function of imaging depth. This spatio-angular distribution of intensity was used to design a maximally efficient post-objective fluorescence collection system. While other low-magnification, high-NA objectives have recently entered the market, we expect the results derived here to be generally applicable. We have demonstrated that efficiently designed systems are capable of collecting significantly more fluorescent signal than conventional geometries, and that this increase in collected fluorescence translates to increased imaging depth, and significantly less required excitation power, which, in turn, results in reduced fluorescence background and potential for photodamage. Significantly, we have shown that, for an optimized system, the fluorescence collection efficiency is only very weakly dependent on imaging depth. Finally, we have demonstrated *in vivo* images of layer V

cell bodies to depth of 850 μm , where we find significant improvements in total collected signal and image contrast.

Acknowledgements

The authors would like to thank Eben Olson for many helpful discussions and coding assistance, and Nathan Gilfoy for surgical and imaging assistance. This publication was made possible by National Center for Research Resources (NCRR) from the Grant Number TL 1 RR024137 and by Grant Number R21EB00770 from the National Institute of Biomedical Imaging and Bioengineering (NIBIB), components of the National Institutes of Health (NIH). Its contents are solely the responsibility of the authors and do not necessarily represent office views of NCRR, NIBIB or NIH.